Bubble Formation in an Annular Granular Jet Dispersed by a Central Air Round Jet

Hui Lu, Hai-Feng Liu, Wei-Feng Li, and Jian-Liang Xu
Key Laboratory of Coal Gasification and Energy Chemical Engineering of Ministry of Education, East China University of Science and Technology, Shanghai 200237, P.R. China

Shanghai Engineering Research Center of Coal Gasification, East China University of Science and Technology, Shanghai 200237, P.R.China

DOI 10.1002/aic.13974
Published online December 26, 2012 in Wiley Online Library (wileyonlinelibrary.com).

An annular granular jet surrounding an air jet at its core is studied experimentally using high-speed digital photography. The experimental results show that particle bubbles in a periodic manner are formed whether the central air is swirling or not. This flow feature is induced by the intense interaction between the central air jet and the annular granular jet, and it is important for the dispersion of particles by the air jet in the near field. The interaction between the two phases is mainly intensified by higher superficial air jet velocity and the addition of swirl to the central air jet. The bubbling frequency, bubble size, bubble shape, and bubble growth rate are investigated by analyzing a large number of images. In addition, the dispersion angle of granular jet is found to be mainly governed by the radial growth rate of the bubble. © 2012 American Institute of Chemical Engineers *AIChE J,* 59: 1882–1893, 2013
Keywords: dense, annular granular jet, gas-particle two-phase flow, swirl, bubble

Introduction

Gas-particle two-phase flows are of great importance for both scientific researches and engineering applications and widely used in various industrial equipments, such as pulverized coal gasifiers[1] and pulverized coal combustors.[2,3] Particle dispersion in two-phase flows, which is one of the most important particle behaviors, is recognized as playing a key role in a wide variety of industrial and energy conversion processes. Thus, the understanding of particle behaviors in the flow field is of considerable importance.

Modarress et al.[4] measured the mean velocity, turbulence intensity of both phases, and the gas-phase turbulent shear stress in two-phase turbulent jets. The results indicated that the presence of the particles reduced the gas velocity fluctuations. Longmire and Eaton[5] examined the behavior of particles in a particle-laden round jet that was forced axially with an acoustic speaker. They found that local particle dispersion and concentration were governed by convection due to large-scale turbulence structures. Sommerfeld and Krebs[6] studied the behavior of the particles in two-phase swirling flow in comparison with the nonswirling case by flow visualization, particle concentration, and velocity measurements. Wicker and Eaton[7,8] experimentally investigated the effect of the recirculation and large-scale vortices on particle dispersion in a swirling, coaxial jet. The results indicated that large-scale vortex rings reduced particle flinging and had effect on the particle distribution. Liu et al.[9,10] experimentally investigated the particle dispersion characteristics of a granular jet surrounded by an annular air jet and identified three dispersion modes, namely, the shear dispersion, wave dispersion, and oscillating dispersion. However, as shown in Table 1, the case with large particle mass loading ratio m (defined as the ratio of the total particle mass flow rate to the air mass flow rate) and swirl is very limited,[8–22] which demonstrates a need for further research on the particle behaviors in dense two-phase flows, including the case with swirl.

In the gasification process of pulverized coal, there are mainly two coaxial jet configurations, namely, the particle-centered type and the gas-centered type. The particle dispersion characteristics of a central granular jet surrounded by an annular air jet have been studied by Liu et al.[9,10] But the study on an annular granular jet dispersed by a central air jet has not been reported. However, a few investigations have been conducted on an annular liquid jet exposed to an inner air jet,[23–29] and several interesting flow features have been observed, for example, the periodic formation of bubbles. Thus, motivated by the research status and future needs, the flow features of an annular granular jet surrounding a central air jet are investigated in this work.

Experimental Setup

The present experiments are conducted with the dense gas-particle coaxial jets directed vertically downward, as shown schematically in Figure 1. Air from a blower continuously passes through a storage tank, a flow meter, a swirler placed in the inner nozzle (for the case with swirl), and finally flows out as the center jet. The storage tank is mainly used to eliminate the disturbance from the blower. High-pressure air supplied by a steel cylinder is used to pressurize the particles stored in a

Correspondence concerning this article should be addressed to H.-F. Liu at hfliu@ecust.edu.cn.

Table 1. Experimental Conditions Under Which Previous Particle-Laden Jet Investigations Were conducted

Researchers	Jet Form	Swirl/No	Particle	d_p (μm)	ρ_p (kg/m^3)	m
Shuen et al.[11]	Premixed	No	Sand particles	79–207	2620	0.2, 0.66
Fleckhaus et al.[12]	Premixed	No	Glass beads	64, 132	2590	0.3
Barlow and Morrison[13]	Premixed	No	Glass beads	163	2825	6.5–54
Longmire and Eaton[15]	Premixed	No	Glass beads	55	2400	0.05–0.11
Sheen et al.[16]	Premixed	No	Polystyrene particles	210–780	1020	0–3.6
Aisa et al.[18]	Premixed	No	Glass spheres	50–100	2450	0.3
Hadinoto et al.[19]	Premixed	No	Glass spheres	70, 200	2500	0.7
Zhou et al.[20]	Premixed	No	Talcum powder	16	2700	0.646
Tamburello and Amitay[21]	Premixed	No	Glass beads	11–50	2500	0.01
Wicker and Eaton[8]*	Coaxial	Swirl	Glass shot	90	2500	0.1
Fan et al.[14,17]*	Coaxial	No	Silica gel powder	50, 200	1250	0–1.5
Mergheni et al.[22]*	Coaxial	No	Glass beads	102–212	—	0.17, 0.7
Liu et al.[9,10]*	Coaxial	No	Glass beads	33.1–183.4	2490	0.7–5.6
This work**	Coaxial	Swirl and no	Glass beads	81–159	2490	5.9–47.3

*A particle jet in a coaxial annular air jet.
**An annular granular jet with a central air jet.

hopper. The hopper is similar to that used in Ref. 9 and connected with the annular channel. A needle valve and a precision pressure gauge are used to monitor the pressure in the hopper and keep it at a constant value. The control method of the particle flow rate is the same as that presented in Ref. 9. In the present experiment, particles discharged from the annular channel are weighed after collection for a timed period to calculate the mass flow rate.

To study the flow field of single air jet, smoke flow visualization is used to capture the instantaneous flow patterns of air jet. The white smoke is used as the flow tracer and generated by some small burning tablets. The flow feature of single air jet and the dispersion process of granular jet are both recorded by a high-speed digital camera (Fastcam, Photron, up to 250,000 frames per seconds [fps] and 10^{-6} s exposure time). In the present experiments, the shooting speed is 1000 fps, and the exposure times of each image for above two cases are 4×10^{-5} and 1.25×10^{-4} s. ImageJ,[30] which is a kind of image processing software, is used to analyze and process the images.

In this study, a coaxial two-channel nozzle has been adopted, as shown schematically in Figure 2a. Air flows through inner channel and particle outer channel. The inner channel of the nozzle, that is, the central channel, has an exit diameter d of 20.0 mm and the outer channel, that is, the annular channel, has an outer diameter D_o of 27.0 mm and an inner diameter D_i of 24.0 mm. Thus, the thickness of the annular channel δ is 1.5 mm. The exits of inner and outer channels are both convergent. The inner one has a convergence angle $\beta = 30°$, whereas the outer one has $\alpha = 70°$.

A guide vane swirler is mounted at $1d$ upstream of the nozzle exit, as marked with dotted line in Figure 2a. Details of swirler are shown in Figure 2b. The degree of swirl for a swirling jet is usually characterized by the swirl number S, which is a dimensionless number representing axial flux of angular momentum to divided by the product of nozzle exit radius and axial flux of axial momentum. The expression of S can be simplified to a number of forms depending on various assumptions.[31] In this work, S is expressed as[32]

$$S = \frac{1 + (R_1/R_2)^2}{2(1-\varphi)} \tan \gamma_0 \tag{1}$$

where R_1 is the radius of the central hub supporting the vanes, R_2 is the external radius of the swirler, and γ_0 is the vane angle at the external edge. In addition, φ is defined as

$$\varphi = \frac{nb}{2\pi R_1 \cos \gamma} \tag{2}$$

where n and b are the number and thickness of the guide vanes, respectively. γ is the established angle of the vanes corresponding to R_1. The relation between γ and γ_0 is given as

$$\tan \gamma = \frac{R_1}{R_2} \tan \gamma_0 \tag{3}$$

Parameters of the three swirlers used in the experiments are listed in Table 2. The Reynolds number of the air is defined as

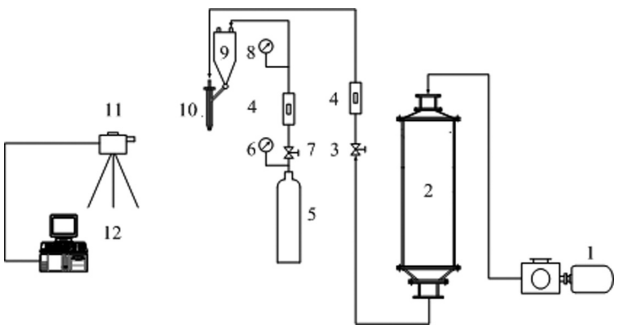

Figure 1. Flow chart of experimental system.

1–blower, 2–storage tank, 3–valve, 4–flow meter, 5–steel cylinder, 6–pressure gauge, 7–needle valve, 8–precision pressure gauge, 9–hopper, 10–coaxial nozzle, 11–high-speed camera, and 12–computer.

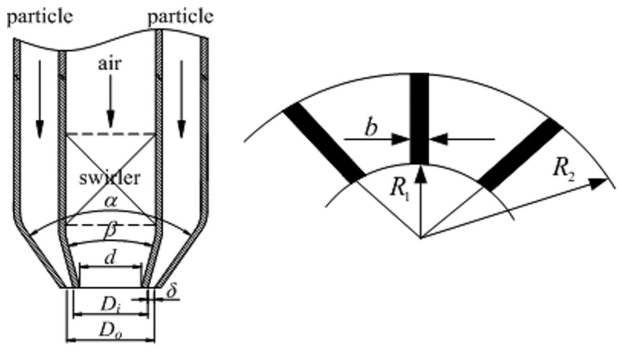

(a) coaxial nozzle (b) swirler

Figure 2. Configuration of coaxial nozzle and schematic diagram of swirler.

Table 2. Geometrical Parameters of Swirlers

Serial number	n	b (mm)	γ_0 (°)	γ (°)	R_1 (mm)	R_2 (mm)	φ	S
Swirler 1	4	2	15	6.37	5	12	0.256	0.21
Swirler 2	4	3	30	21.1	8	12	0.256	0.56
Swirler 3	4	3	45	33.7	8	12	0.287	1.01

$$Re = \frac{du_{g0}\rho_g}{\mu_g} \tag{4}$$

where u_{g0}, ρ_g, and μ_g are the superficial air jet velocity, density, and dynamic viscosity of the air, respectively. The superficial air jet velocity is defined as the mean velocity of the air from the central channel.

Spherical glass beads used as the particle phase are of three sizes: 81, 125, and 159 μm. The particle mass flow rate is $m_p = 0.041$ kg/s. Thus, the superficial particle jet velocity that represents the mean velocity of the particle from the annular channel is given by

$$u_{p0} = \frac{m_p}{\frac{\pi}{4}\rho_b(D_o^2 - D_i^2)} = 0.234\,\mathrm{m/s} \tag{5}$$

where ρ_b is the bulk density of the particle. The particle mass loading ratio m varies from 5.9 to 47.3. The Stokes number of particle is defined as

$$St = \tau_p/\tau_g = \frac{d_p^2\rho_p/18\mu_g}{d/u_{g0}} \tag{6}$$

where τ_p and τ_g are the aerodynamic response time of a particle and the air timescale, respectively. d_p and ρ_p are the diameter and density of the particle, respectively. The Strouhal number of the bubble-formation process is defined as

$$Sr = \frac{f_b d}{u_{g0}} \tag{7}$$

where f_b is the bubbling frequency. The detailed experimental conditions of the air and particles are contained in Table 3.

Results and Discussion

Bubble characteristics in the bubbling fluidized bed such as bubble size, shape, and bubble rise velocity are very important for the design of gas–solid fluidized beds and optimizing the rate of mass transfer, heat transfer, and chemical reactions.[33] In view of the above, numerous studies focused on the bubble behavior in fluidized bed have been conducted.[34–39] Similar to the bubble at the top of the fluidized bed,[33] a noticeable "particle bubble" (hereinafter referred to as "bubble") is also observed in this work. The features of the bubble presented herein are shown in the following sections.

Table 3. Experimental Parameters of Gas Phase (Air) and Particle Phase (Glass Beads)

Phase	Parameters	
Gas (air)	Superficial air jet velocity u_{g0} (m/s)	2.21–17.7
	Air dynamic viscosity μ_g (μPa s)	17.9
	Air density ρ_g (kg/m^3)	1.247
	Swirl number, S	0, 0.21, 0.56, 1.01
	Reynolds number, Re	3079–24,661
Particle (glass beads)	Particle diameter, d_p (μm)	81, 125, 159
	Particle density, ρ_p (kg/m^3)	2490
	Particle bulk density, ρ_b (kg/m^3)	1460
	Superficial particle jet velocity, u_{p0} (m/s)	0.234
	Particle mass flow rate, m_p (kg/s)	0.041
	Particle mass loading ratios, m	5.9–47.3
	Particle volume fraction (%)	0.3–2.3
	Stokes number, St	5.6–172.9

Bubbling phenomenon of annular granular jet

The flow patterns of the annular granular jet with a nonswirling central air for different u_{g0} are shown in Figure 3. For $u_{g0} < 4.42$ m/s, the granular jet is vertically downward, as shown in Figure 3a. In this case, aerodynamic forces are not sufficient to change the flow pattern. When $u_{g0} = 4.42$ m/s, the granular jet becomes strongly periodic within a short distance from the nozzle exit, that is, a "particle bubble" chain is formed (see Figure 3b). As shown in Figure 3b, the initial bubble is regular in shape; nevertheless, it bursts while propagating downstream. With a further increase of u_{g0} ($u_{g0} > 4.42$ m/s), the distinct bubble disappears gradually, but the initial bubble is still identifiable (Figures 3c,d). The radial dispersion of particles is more prominent for higher u_{g0}; however, the bubbles become more irregularly shaped and easier to burst.

Similarly, Figures 3e–h illustrates the flow patterns of the annular granular jet with a swirling central air for different u_{g0}. Compared with the flow pattern shown in Figure 3a, the granular jet is falling downward along a spiral trajectory for $u_{g0} < 4.42$ m/s, as illustrated in Figure 3e. With the increase of u_{g0}, it is observed that a chain of bubbles in a periodic manner is also formed (Figure 3f), but the shape of the bubbles is less regular than that shown in Figure 3b. Due to the aerodynamic shear, the bubbles are torn off while propagating downstream. With a further increase of u_{g0}, the distinct bubbles disappear gradually, but the initial bubble is still observable, as shown in Figures 3g,h. Meanwhile, the bubble is progressively shortened along the axial direction and elongated along the radial direction. Compare to the case with a nonswirling central air, more evenly dispersion of particles is achieved, which is considered to be due to centrifugal effects and strong interaction between the granular jet and the swirling air jet.

Bubble-formation process

As mentioned earlier, the bubble is periodically formed within a certain range of u_{g0}. The morphological feature of the bubble is similar to the multiple converging sections studied by Sivakumar and Raghunandan.[27] To study the bubble-formation process, Figure 4 illustrates the flow patterns of central air jet with and without swirl by smoke flow visualization. Obviously, the bubble is not formed in the single air jet whether the center air is swirling or not. However, noticeable bubbles appear in the near field for the two-phase flows with and without swirl (Figures 3b,f). Consequently, the interaction between the annular granular jet and the

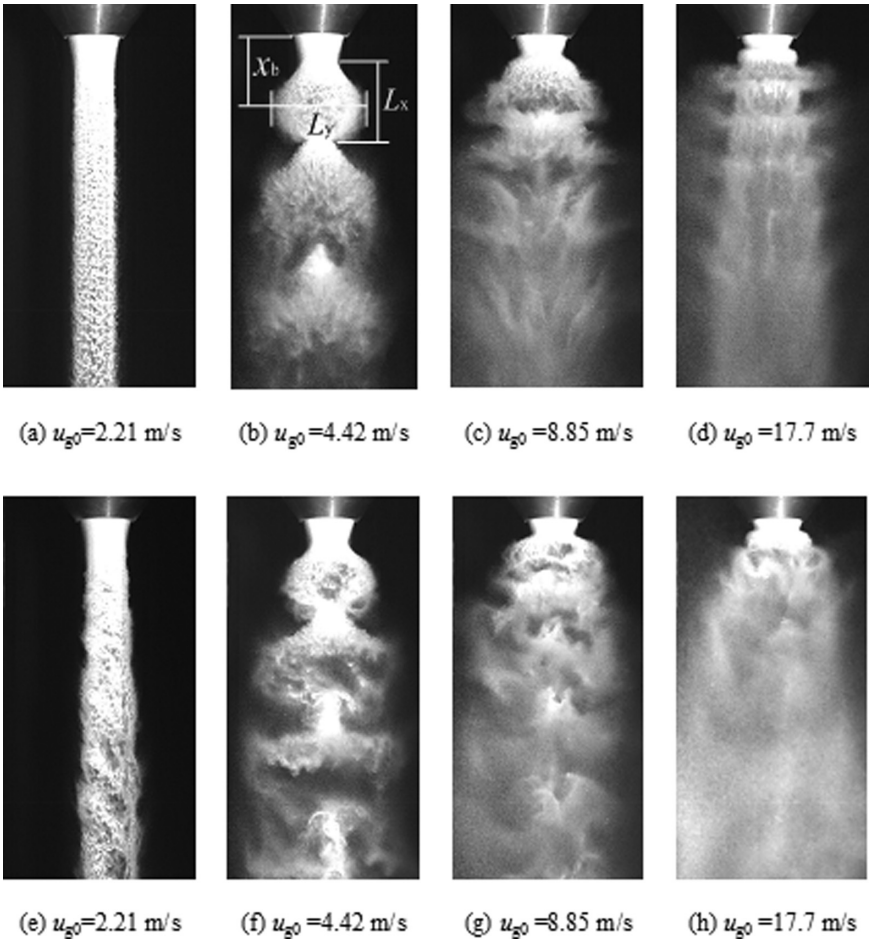

Figure 3. The evolution of flow patterns of granular jet with the increase of u_{g0}.

(a–d) $d_p = 81$ μm, $S = 0$ and (e–h) $d_p = 81$ μm, $S = 1.01$.

central air jet is considered to be the precondition that triggers the formation of bubbles.

In this study, the interaction between the gas and particle phases is mainly intensified by the addition of swirl to the central air jet and the increase of superficial air jet velocity. As illustrated in Figures 3b,f, the bubbles both appear when u_{g0} exceeds 4.42 m/s, and the difference in shape of the initial bubble between the two cases is not significant. So, we can conclude that swirl is not the vital influence factor in the bubble-formation process. However, with the increase of superficial air jet velocity (see Figure 3), an irregularly shaped bubble, rather than a bubble chain, is formed. The above observation indicates that the increase of superficial air jet velocity, which results in more intense interaction between the gas and particle phases, seriously influences the appearance of the bubbles.

Similar to the formation of gas-filled liquid bubbles described by Kendall,[23] the formation of the above-mentioned bubble is described as follows. Figure 5 illustrates the time-sequence pictures of the bubble-formation process for the cases with and without swirl. As the inner and outer nozzles used herein are both convergent, the granular jet converges toward the jet axis on account of the inertia, thereby forming a neck, as marked with arrow in Figures 5a,e. Similar to what happens in the water-hammer phenomenon, the rapid contraction of the neck will give rise to a compression

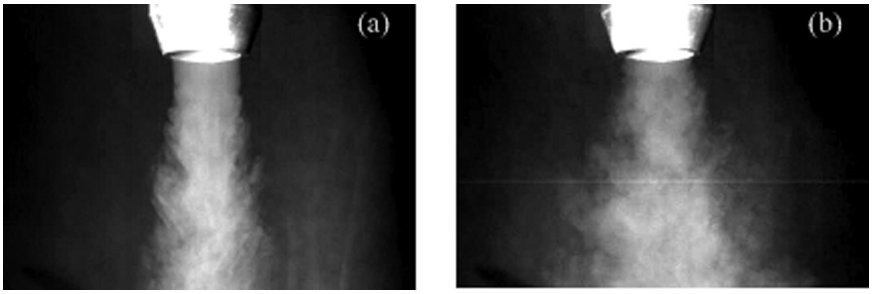

Figure 4. The flow patterns of single air jet in the near field observed by smoke flow visualization.

(a) $S = 0$, $u_{g0} = 4.42$ m/s and (b) $S = 1.01$, $u_{g0} = 4.42$ m/s.

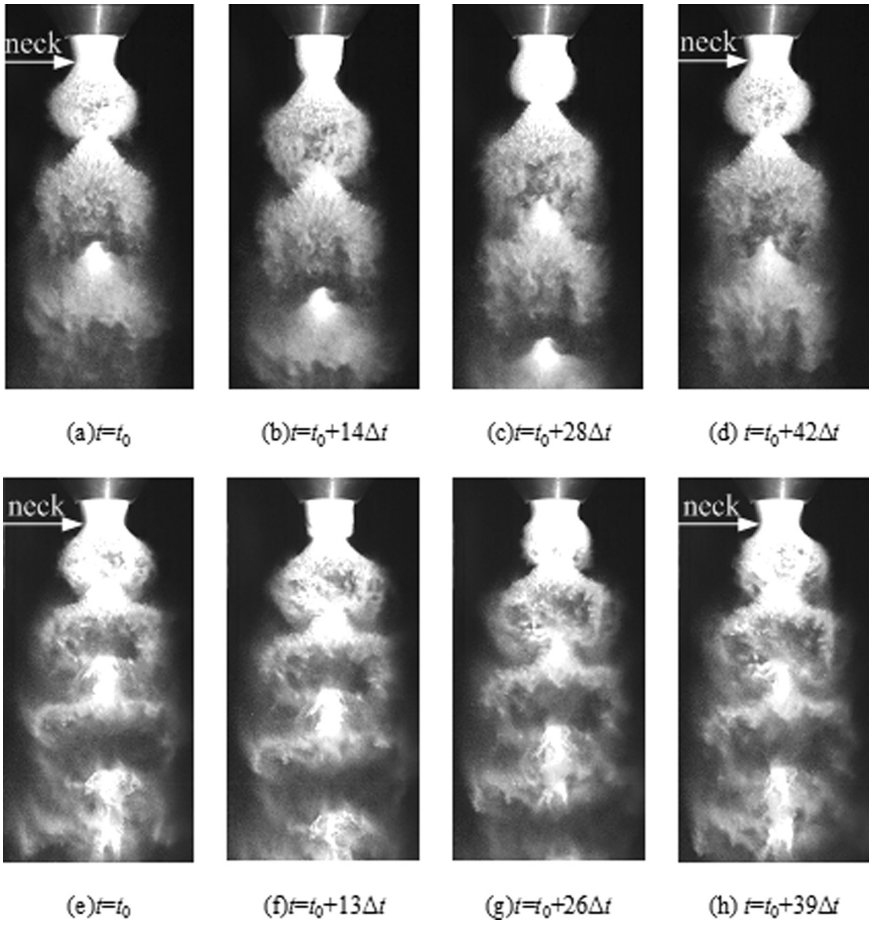

Figure 5. The time-sequence images illustrating the formation of bubbles (Δt = 0.001 s).

(a–d) $S = 0$, $d_p = 81$ μm, $u_{g0} = 4.42$ m/s and (e–h) $S = 1.01$, $d_p = 81$ μm, $u_{g0} = 4.42$ m/s.

wave that causes a sudden increase of the air pressure inside the granular jet. Because of the pressure difference across the granular jet (ΔP), a radial displacement of the annular granular jet appears (Figures 5b,f). Afterward, the bubble feature becomes gradually noticeable (Figures 5c,g). With further expansion of the granular jet, the next neck emerges again (Figures 5d,h), completing the formation of the first complete bubble. Subsequently, the next bubbling period starts, repeating the same sequences of events as described earlier. As mentioned earlier, the periodic fluctuations of the pressure difference across the granular jet, which are raised by the interaction between the central air jet and the annular granular jet, are responsible for the formation of bubbles.

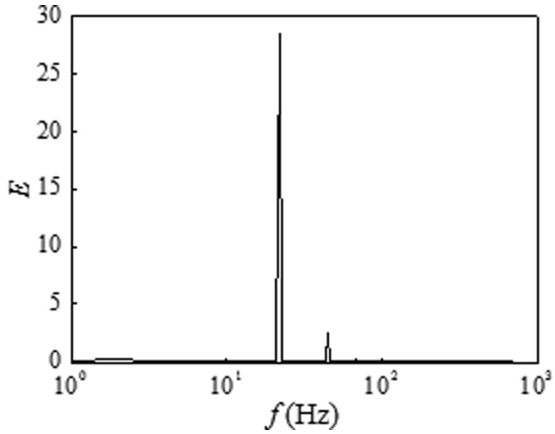

Figure 6. Power spectrum of the half-width of the granular jet ($S = 0$, $d_p = 81$ μm, u_{g0}=4.42 m/s).

Bubbling frequency

The bubbling frequency f_b is an important characteristic scale in the bubble-formation process. It is calculated by a procedure, which uses edge detection algorithm and Fourier transform algorithm, and the edge detection algorithm is used to search the half-width of the granular jet in the near field. Take the case without swirl as an example, Figure 6 presents the spectrum of half-width for $u_{g0} = 4.42$ m/s. A sharp spectral peak is observed, which indicates that a characteristic frequency exists in the bubble-formation process. In addition, the power spectra of the single air velocity at the nozzle exit are given in Figure 7. Obviously, a sharp spectral peak is also observed in the case with disturbance of blower (no storage tank), which suggests that the air from the blower has a frequency of 39.8 Hz (Figure 7a). However, as shown in Figure 7b, this frequency disappears when the storage tank is added to the experimental system, which demonstrates that the disturbance of blower has been eliminated effectively. Thus, the above characteristic frequency (observed in Figure 6) is considered as a natural frequency of bubble-formation process.

The variation in f_b with u_{g0} for different swirl numbers is given in Figure 8a. Clearly, f_b increases rapidly with u_{g0}, which indicates that f_b is strongly dependent on u_{g0}. Similar to the results shown in Ref. 23, the growth of f_b with u_{g0} is

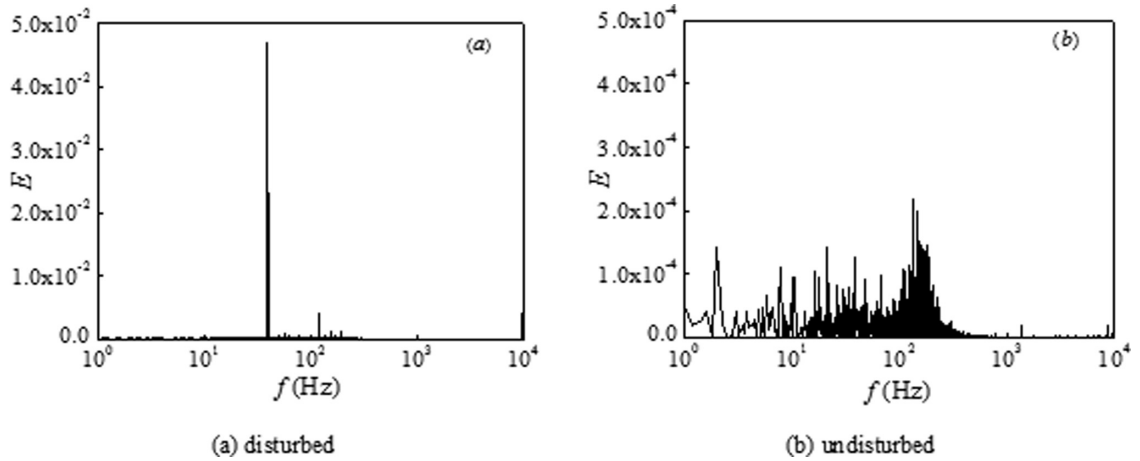

Figure 7. Power spectrum of single air velocity with and without disturbance of blower ($u_{g0} = 4.42$ m/s, $S = 0$).

nearly linear when S remains constant. However, the formation frequency of the liquid bubble[23] is much larger than the bubbling frequency studied herein. In addition, it is also observed that f_b increases with S. The above results suggest that strong swirl and high superficial air jet velocity can promote the formation of bubbles. Figure 8b presents f_b varied with u_{g0} for different particle sizes. Note that f_b increases slightly with d_p, which indicates that d_p has only a slight influence on f_b in comparison with u_{g0}.

According to the above experimental results, a dimensionless correlation of the bubbling frequency related with swirl number, Stokes number, and Reynolds number is given by

$$Sr = 2.12(1 + 2.79S)^{0.156} St^{0.0755} Re^{-0.377} \quad (8)$$

Equation 8 is accurate within 3.2% (mean of relative error). According to Eqs. 4, 6, and 7, the expression of St contains both d_p and u_{g0}, and the expressions of Re and Sr contain only u_{g0}. The exponents of variables in Eq. 8 suggest that the influence of u_{g0} on f_b is more significant than that of S and d_p. The values of Sr calculated with Eq. 8 against those measured experimentally are illustrated in Figure 9.

Dynamical evolution of the bubble

In this work, the trajectory of the initial bubbling distance, the axial and radial bubble size, that is, $x_b(t)$, $L_x(t)$ and $L_y(t)$, are experimentally measured for different swirl numbers, particle sizes, and superficial air jet velocities. As illustrated in Figure 3b, x_b denotes the initial bubbling distance that is defined as the axial distance between the plane of nozzle exit and the central plane of the first bubble. In addition, L_x and L_y denote the axial and radial bubble size, respectively.

Some of the detailed measurements are shown in Figure 10. Notice that the time evolution of x_b, L_x, and L_y are periodic for the case of $S = 0$, $u_{g0} = 4.42$ m/s, and $d_p = 81$ μm. And similar results are also observed in the cases with different swirl numbers, superficial air jet velocities and particle sizes. Because of limitations of space, no need to repeat them here. Besides, an important conclusion that can be extracted from Figure 10 is that, as the time evolution of x_b, L_x, and L_y are practically linear during each bubbling period and the slopes of lines for a given condition are almost the same value, the bubbling velocity (u_b) and the axial and radial growth rates of the first bubble (u_x and u_y) are nearly constant for a given condition. It should be mentioned here that u_x and u_y are both relative values, whereas u_b is the absolute velocity of bubbling. The above observation suggests that, when swirl number, particle size, and superficial air jet velocity keep constant, the bubbling velocity and the growth rates of the initial bubble in both directions also remain constant.

Figure 11 presents the time evolution of the dimensions ratio of the initial bubble during a bubbling period T. It can

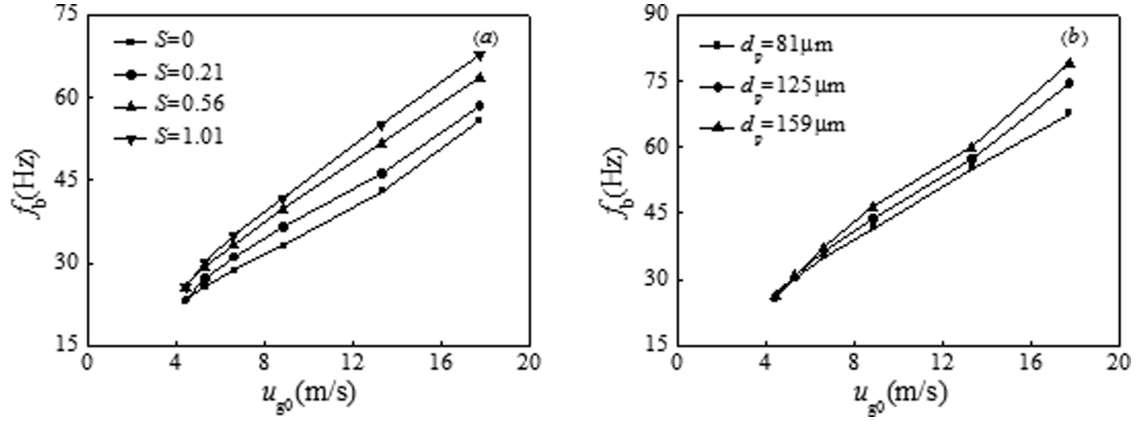

Figure 8. The variation in f_b with u_{g0} for different swirl numbers and different particle sizes.

(a) 4.42 m/s $\le u_{g0} \le$ 17.7 m/s, $d_p = 81$ μm and (b) 4.42 m/s $\le u_{g0} \le$ 17.7 m/s, $S = 1.01$.

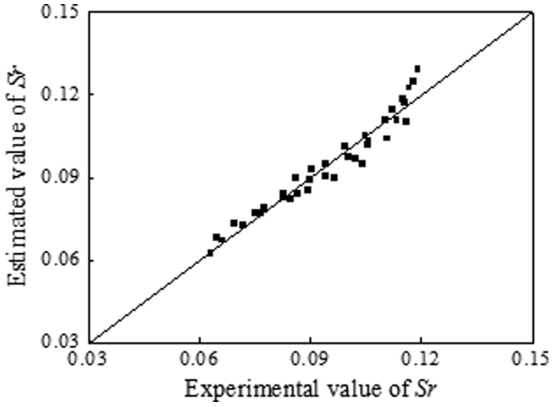

Figure 9. Comparison between the experimental results and estimated results of *Sr*.

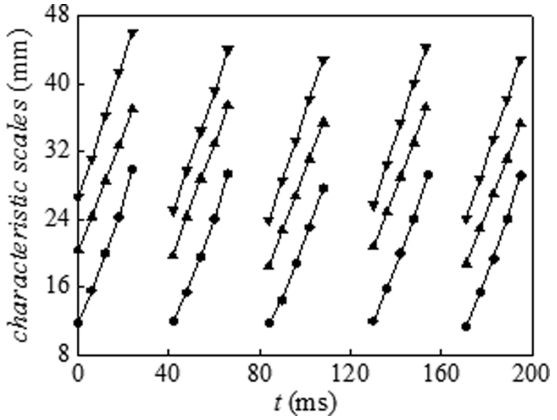

Figure 10. Time evolution of the characteristic scales for $S = 0$, $u_{g0} = 4.42$ m/s, $d_p = 81$ μm.

●: x_b; ▲: L_x; and ▼: L_y.

be observed that L_y/L_x increases with u_{g0}, S, and d_p, which indicates that high superficial air jet velocity, strong swirl, and large particle size can intensify the deformation of initial bubble. In addition, the dimensions ratios of initial bubble exceed 1 under various conditions, which implies that the bubble is not exactly spherical but rather shaped like a flattened ellipsoid. As mentioned earlier, L_x and L_y both increase linearly with t. However, L_y/L_x is found to decrease nonlinearly with t, which suggests that the growth rate of L_y is smaller than that of L_x.

L_{xe} and L_{ye} are defined as the bubble size in both directions at the end of the bubble-formation period. Figure 12 shows L_{xe} and L_{ye} varied with u_{g0} for different swirl numbers. Note that L_{xe} decreases rapidly with the increase of S and u_{g0}, whereas L_{ye} increases with S and u_{g0}. This observation implies that the bubble is extremly deformed in shape by strong swirl number and high superficial air jet velocity. Figure 13 shows L_{xe} and L_{ye} varied with u_{g0} for different particle sizes. Clearly, L_{xe} and L_{ye} both decrease with the increase of d_p, which indicates that the expansion of the bubble in both directions for large particles is not as noticeable as that for small particles. This phenomenon may be due to the large inertia and poor following behavior of the large particles.

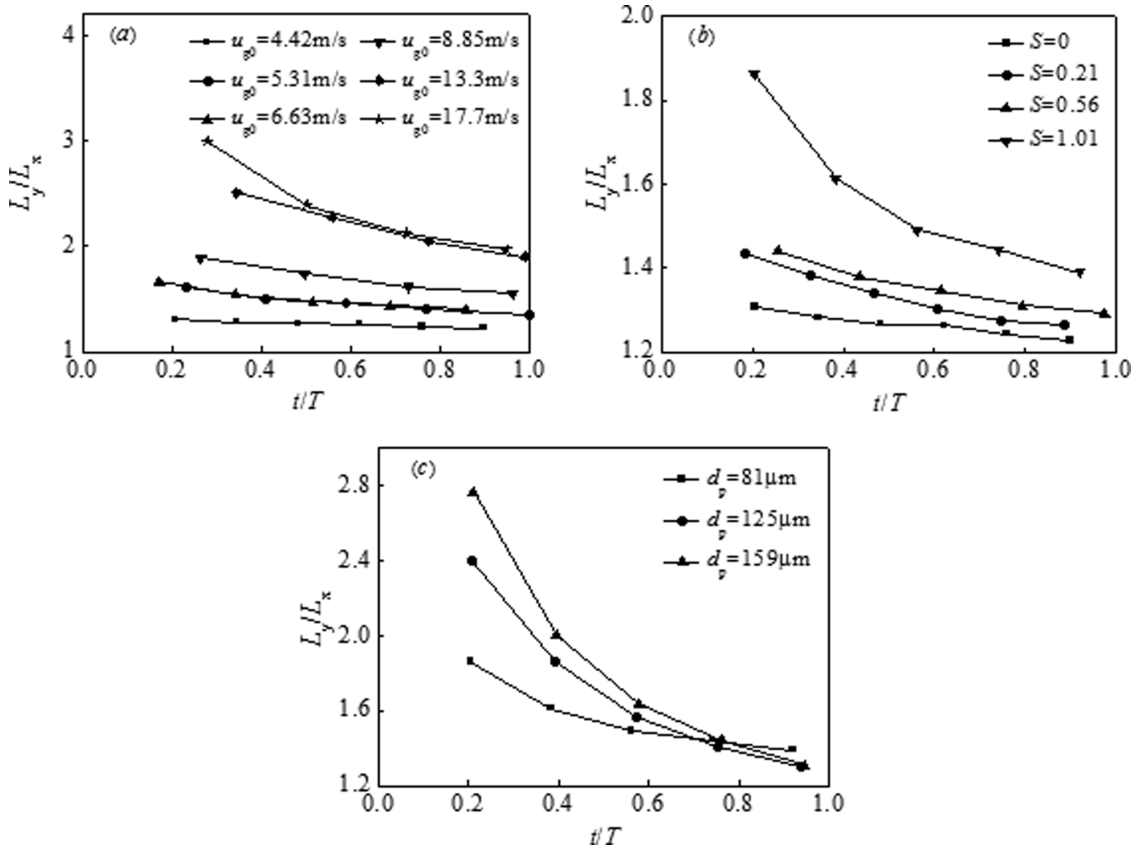

Figure 11. Time evolution of the dimensions ratio of the initial bubble L_y/L_x for different u_{g0}, S, and d_p.

(a) $S = 0$, $d_p = 81$ μm; (b) $u_{g0} = 4.42$ m/s, $d_p = 81$ μm; and (c) $S = 1.01$, $u_{g0} = 4.42$ m/s.

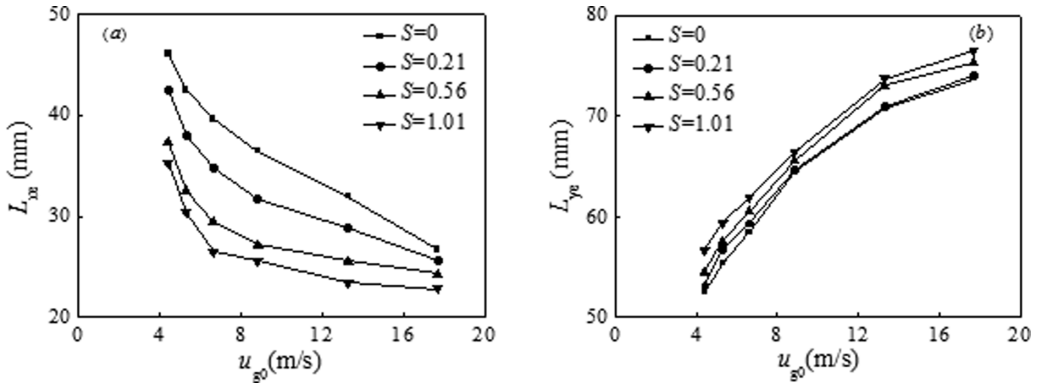

Figure 12. The variation in L_{xe} and L_{ye} with u_{g0} for different swirl numbers (4.42 m/s $\leq u_{g0} \leq$ 17.7 m/s, d_p = 81 μm).

(a) L_{xe} and (b) L_{ye}.

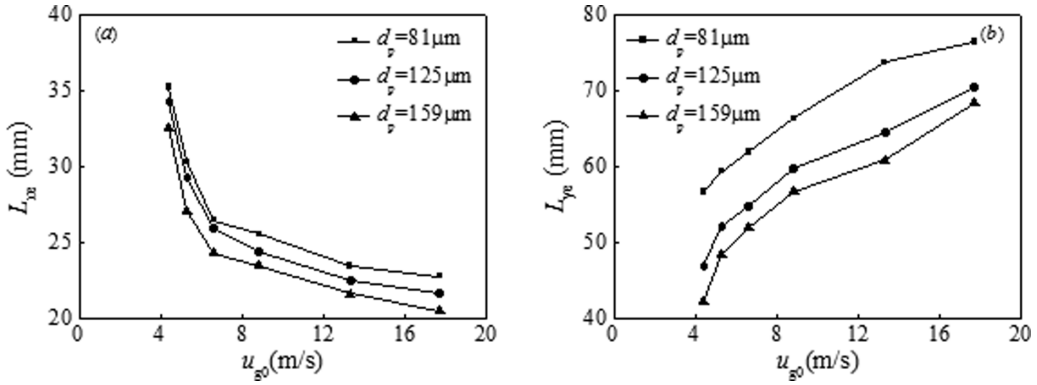

Figure 13. The variation in L_{xe} and L_{ye} with u_{g0} for different particle sizes (4.42 m/s $\leq u_{g0} \leq$ 17.7 m/s, S = 1.01).

(a) L_{xe} and (b) L_{ye}.

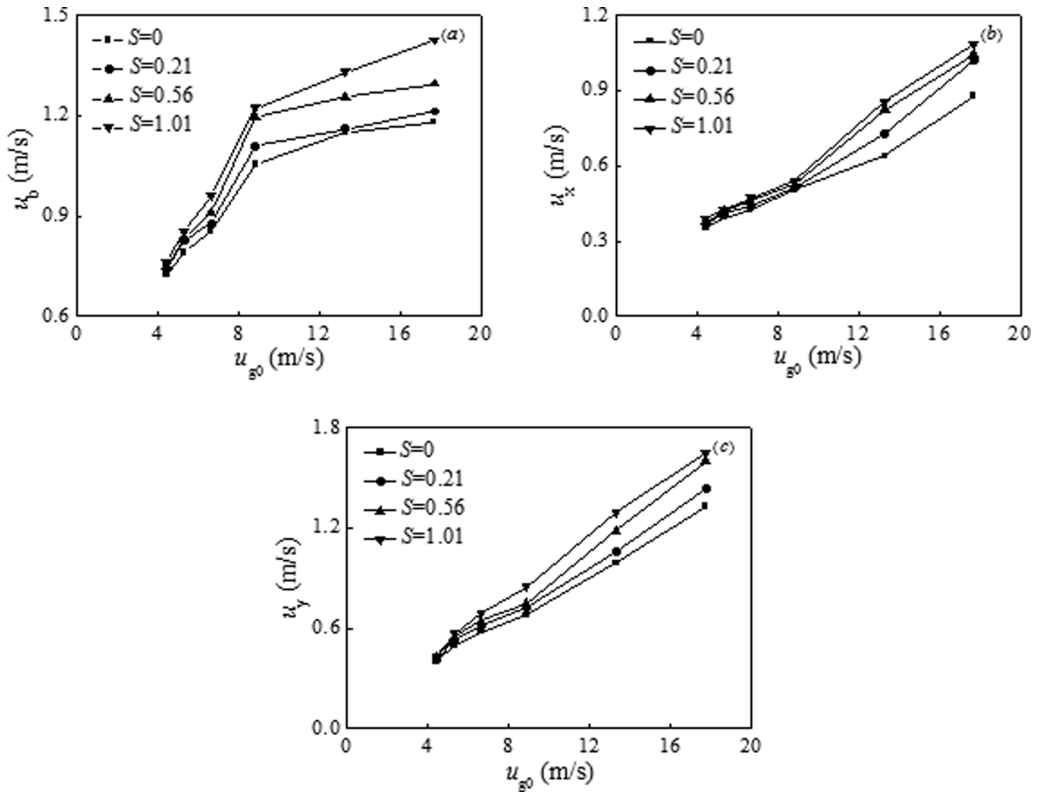

Figure 14. The variation of u_b, u_x, and u_y with u_{g0} for different swirl numbers (d_p = 81 μm).

(a) u_b, (b) u_x, and (c) u_y.

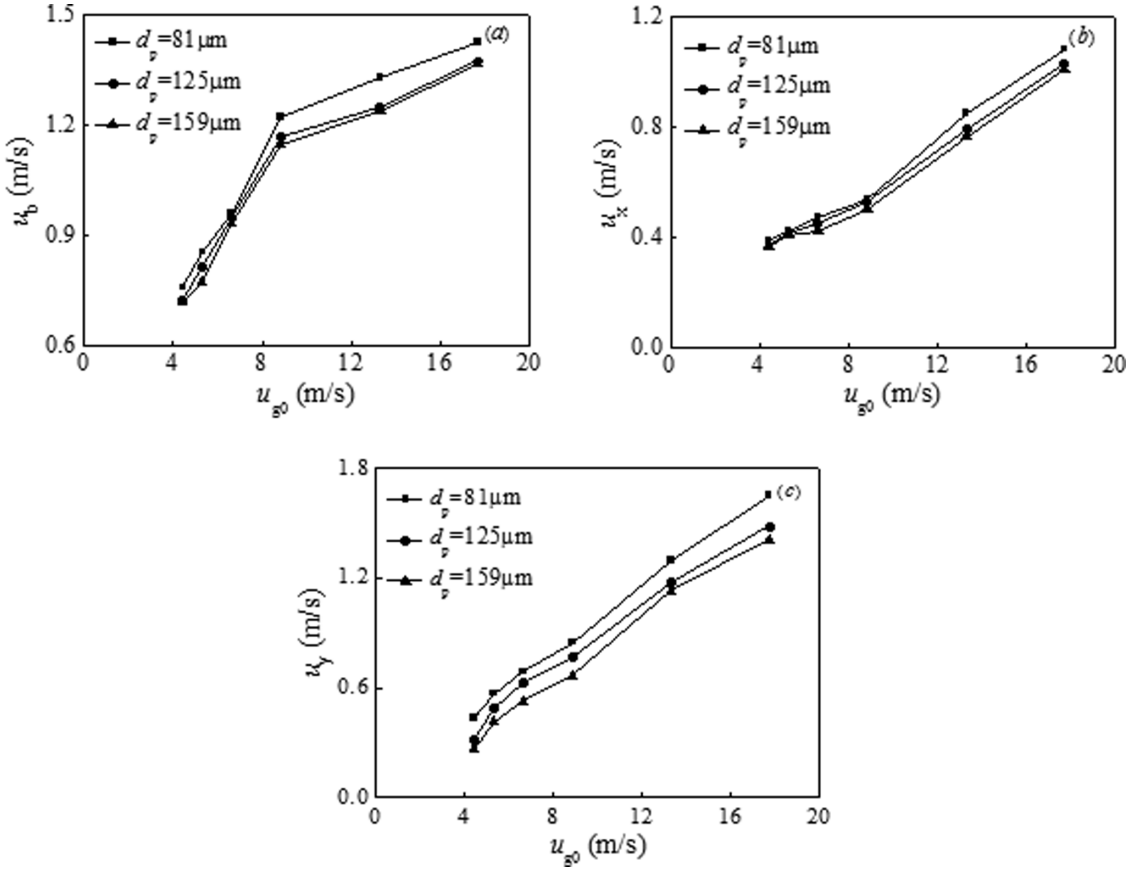

Figure 15. The variation of u_b, u_x, and u_y with u_{g0} for different particle sizes ($S = 1.01$).

(a) u_b, (b) u_x, and (c) u_y.

According to the above results, a dimensionless correlation of L_{xe} related with swirl number, Stokes number, and Reynolds number is expressed as

$$\frac{L_{xe}}{D_o} = 22.1(1 + 2.92S)^{-0.232} St^{-0.0542} Re^{-0.280} \quad (9)$$

Equation 9 is accurate within 4.1%. The exponents of variables in Eq. 9 indicate that L_{xe} is slightly dependent on d_p. Similarly, a dimensionless empirical correlation of L_{ye} is given by

$$\frac{L_{ye}}{D_o} = 0.0981(1 + 2.92S)^{0.0353} St^{-0.131} Re^{0.379} \quad (10)$$

Figure 16. Schematic diagram of the dispersion angle (100 superimposed images, $\Delta t = 0.001$ s).

Equation 10 is accurate within 1.6%. The exponents of variables in Eq. 10 indicate that L_{ye} is slightly dependent on S.

Figure 14 illustrates u_b, u_x, and u_y varied with u_{g0} for different swirl numbers. Note that u_b, u_x, and u_y increase with u_{g0} and S. As shown in Figure 14a, u_b behaves a slow increase with u_{g0}. However, as illustrated in Figures 14b,c, the variations of u_x and u_y with u_{g0} are nearly linear. The above results reveal that the increase of u_{g0} and S can effectively promote the growth of the bubble. Figure 15 shows u_b, u_x, and u_y varied with u_{g0} for different particle sizes. It is observed that u_b, u_x, and u_y all decrease with the increase of d_p.

Thus, a dimensionless correlation of the bubbling velocity obtained from the experimental results is written as

$$\frac{u_b}{u_{p0}} = 0.0755(1 + 2.92S)^{0.102} St^{-0.0380} Re^{0.436} \quad (11)$$

Equation 11 is accurate within 4.7%. The exponents of variables in Eq. 11 demonstrate that u_b is weakly dependent on d_p.

As mentioned earlier, a compression wave raises an overpressure ΔP, which results in an instantaneous expansion of the granular jet. According to Joukowsky's fundamental equation of water hammer,[40] the overpressure ΔP is approximately proportional to $(u_{g0} - u_{p0})$. As $u_{g0} > u_{p0}$, we have

$$\Delta P \propto u_{g0} \quad (12)$$

The expansion of the granular jet is similar to the explosion process to a certain extent. According to the impulse-momentum

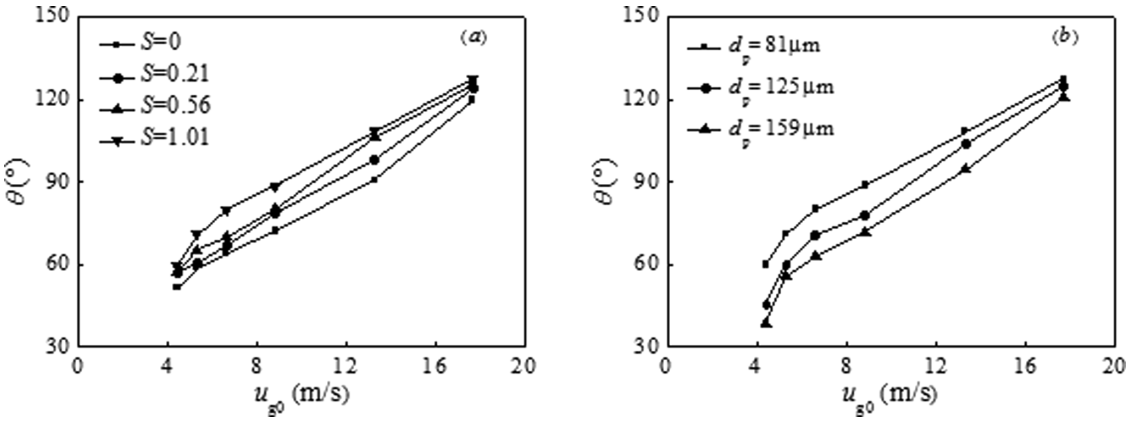

Figure 17. The variation in θ with u_{g0} for different swirl numbers and different particle sizes.

(a) 4.42 m/s $\leq u_{g0} \leq$ 17.7 m/s, $d_p = 81$ μm and (b) 4.42 m/s $\leq u_{g0} \leq$ 17.7 m/s, $S = 1.01$.

theorem, the pressure force impulse of the air is converted into the momentum of the granular jet at the instant of expansion. Thus, we have

$$\Delta P A_x \tau \propto m_{p0} u_x \tag{13}$$

and

$$\Delta P A_y \tau \propto m_{p0} u_y \tag{14}$$

where τ is the acting time of the pressure force, and m_{p0} is the mass of particle group. A_x and A_y denote the acting areas of the pressure force in both directions. The acting time τ is so short that all the other external forces acting on the granular jet can be ignored. Consequently, u_x and u_y will remain constant. Thus, we can conclude that

$$u_x \propto \Delta P \propto u_{g0} \tag{15}$$

and

$$u_y \propto \Delta P \propto u_{g0} \tag{16}$$

According to the above experimental results, the axial and radial growth rates of the first bubble are related with swirl number, Stokes number, and Reynolds number by

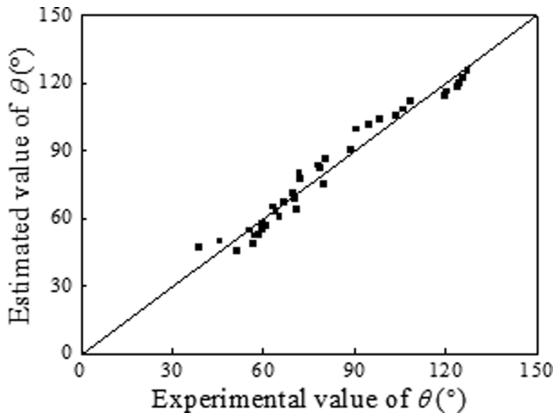

Figure 18. Comparison between the experimental results and estimated results of the dispersion angle.

$$\frac{u_x}{u_{p0}} = 8.95 \times 10^{-4}(1 + 2.92S)^{0.130} St^{-0.0669} Re^{0.852} \tag{17}$$

and

$$\frac{u_y}{u_{p0}} = 1.77 \times 10^{-4}(1 + 2.92S)^{0.164} St^{-0.138} Re^{1.08} \tag{18}$$

Equations 17 and 18 are accurate within 6.2 and 6.1%, respectively. According to Eqs. 4 and 6, the exponents of variables in Eqs. 17 and 18 demonstrate that u_x and u_y are both strongly dependent on u_{g0}, which agree well with $u_x \propto u_{g0}$ and $u_y \propto u_{g0}$.

Dispersion angle

The dispersion angle of the granular jet is an important parameter in quantitative characterizing the dispersion characteristics of the particles. Similar to the definition of spray angle in the liquid jet,[41] dispersion angle θ is defined as the largest angle formed by the cone of particles discharged from the annular channel and measured by the image processing software ImageJ. As shown schematically in Figure 16, the dispersion angle is obtained by superimposing each one hundred images in turn, and the time interval Δt between images is 0.001 s.

The variation in θ with u_{g0} for different swirl numbers is presented in Figure 17a. It is observed that θ increases monotonously with S and u_{g0}. In addition, Figure 17b presents θ varied with u_{g0} for different particle sizes. However, θ decreases with the increase of d_p, which is due to the poor following behavior of large particles. The above observations reveal that strong swirl, high superficial air jet velocity, and small particle size can raise large dispersion angle and, thus, improve the dispersion of particles.

According to the schematic diagram and definition of the dispersion angle, we can conclude that the dispersion angle is mainly dependent on the sudden radial expansion at the nozzle exit, which is characterized by the radial growth rate of the first bubble. Thus, we have

$$\tan\frac{\theta}{2} \propto u_y \tag{19}$$

and with Eq. 18, yielding

$$\theta = 2\arctan\left[C(1+2.92S)^{0.164}St^{-0.138}Re^{1.08}\right] \quad (20)$$

where C is a constant. According to Eqs. 4 and 6, an empirical correlation obtained from the experimental results is given by

$$\theta = 2\arctan\left[4.71\times10^{-5}(1+2.92S)^{0.164}St^{-0.138}Re^{1.08}\right] \quad (21)$$

Equation 21 is accurate within 6.1%, which demonstrates that above conclusion on the dispersion angle is reasonable. Equation 21 also suggests that θ is highly dependent on u_{g0}. The values of θ calculated with Eq. 21 against those measured experimentally are illustrated in Figure 18.

Conclusions

In this article, the dispersion characteristics of dense granular jet exposed to central air jets with and without swirl have been studied by high-speed camera. It is observed that the bubbles in a periodic manner are formed whether the central air is swirling or not. Detailed analysis reveals that the bubble-formation process is induced by the interaction between the central air jet and the annular granular jet. High superficial air jet velocity and the addition of swirl to the central air are major factors that can intensify interaction between the two phases. In comparison with the swirl, the superficial air jet velocity seriously influences the appearance of the bubbles.

By analyzing a large number of images, several characteristic scales (e.g., bubbling frequency, bubble size, bubble growth rate, and dispersion angle) are obtained and well predicted by a series of dimensionless correlations. The dimensions ratio of the initial bubble suggests that the bubble is not exactly spherical but rather shaped like a flattened ellipsoid. In addition, the dispersion angle is found to be controlled by the radial growth rate of the bubble, which reveals that, in the near field, the formation of the bubble has a significant influence on particle dispersion.

Acknowledgments

This research was supported by the National Basic Research Program of China (2010CB227005) and National Natural Science Foundation of China (20906020).

Notation

Roman letters

A_x, A_y = axial and radial acting areas of the overpressure in the bubble, m^2
b = thickness of the guide vanes, m
d = central channel diameter of the nozzle, m
d_p = particle diameter, μm
D_i, D_o = inner and outer diameters of the annular channel of the nozzle, m
f_b = bubbling frequency, Hz
L_x, L_y = axial and radial bubble size, m
L_{xe}, L_{ye} = axial and radial bubble size at the end of the bubble-formation period, m
m = particle mass loading ratio
m_p = particle mass flow rate, kg/s
n = number of the guide vanes
ΔP = pressure difference across the granular jet, Pa
R_1 = radius of the central hub, m
R_2 = external radius of the swirler, m
Re = Reynolds number
S = swirl number
Sr = Strouhal number
St = Stokes number
t = time, s
t_0 = initial time of bubbling, s
Δt = time interval, s
T = bubbling period
u_b = bubbling velocity, m/s
u_x, u_y = axial and radial growth rates of the first bubble, m/s
u_{g0} = superficial air jet velocity, m/s
u_{p0} = superficial particle jet velocity, m/s
x_b = initial bubbling distance, m

Greek letters

α = convergence angle of outer nozzle, °
β = convergence angle of inner nozzle, °
γ = established angle of the vane, °
γ_0 = vane angle at the external edge, °
δ = thickness of the annular channel of the nozzle, m
θ = dispersion angle, °
μ_g = air dynamic viscosity, Pa s
ρ_b = particle bulk density, kg/m^3
ρ_g = air density, kg/m^3
ρ_p = particle density, kg/m^3
τ = acting time of the overpressure in the bubble, s
τ_g = air timescale
τ_p = aerodynamic response time of a particle, s
φ = obstruction coefficient

Subscripts

b = bubble
g = gas
p = particle
x = axial coordinate
y = radial coordinate

Literature Cited

1. Dai ZH, Gong X, Guo XL, Liu HF, Wang FC, Yu ZH. Pilot-trial and modeling of a new type of pressurized entrained-flow pulverized coal gasification technology. *Fuel*. 2008;87:2304–2313.
2. Zhang J, Zhou LX. Particle behaviors in a pulverized coal-fired sudden-expansion combustor with coaxial jets. *Fuel*. 2001;80:289–299.
3. Chen ZC, Li ZQ, Jing JP, Chen LZ, Wu SH, Yao Y. Gas/particle flow characteristics of two swirl burners. *Energy Convers Manage*. 2009;50:1180–1191.
4. Modarress D, Tan H, Elghobashi S. Two-component LDA measurement in a two-phase turbulent jet. *AIAA J*. 1984;22:624–630.
5. Longmire EK, Eaton JK. Structure of a particle-laden round jet. *J Fluid Mech*. 1992;236:217–257.
6. Sommerfeld M, Krebs W. Particle dispersion in a swirling confined jet flow. *Part Part Syst Charact*. 1990;7:16–24.
7. Wicker RB, Eaton JK. Structure of a swirling, recirculating coaxial free jet and its effect on particle motion. *Int J Multiphase Flow*. 2001;27:949–970.
8. Wicker RB, Eaton JK. Effect of injected longitudinal vorticity on particle dispersion in a swirling, coaxial jet. *ASME Trans J Fluids Eng*. 1999;121:766–772.
9. Liu HF, Cao WG, Xu JL, Li WF, Sun ZG. Dispersion mode of granular jet in a coaxial air jet. *Powder Technol*. 2012;217:566–573.
10. Liu HF, Cao WG, Xu JL, Li WF, Guo XL, Sun ZG. Characterization of the granular jet in a coaxial gas stream. *Powder Technol*. 2012;225:206–213.
11. Shuen JS, Solomon ASP, Zhang QF, Faeth GM. Structure of particle-laden jets: measurements and predictions. *AIAA J*. 1985;23:396–404.
12. Fleckhaus D, Hishida K, Maeda M. Effect of laden solid particles on the turbulent flow structure of a round free jet. *Exp Fluids*. 1987;5:323–333.
13. Barlow RS, Morrison CQ. Two-phase velocity measurements in dense particle-laden jets. *Exp Fluids*. 1990;9:93–104.
14. Fan JR, Zhao H, Cen KF. An experimental study of two-phase turbulent coaxial jets. *Exp Fluids*. 1992;13:279–287.
15. Longmire EK, Eaton JK. Active open-loop control of particle dispersion in round jets. *AIAA J*. 1994;32:555–563.
16. Sheen HJ, Jou BH, Lee YT. Effect of particle size on a two-phase turbulent jet. *Exp Therm Fluid Sci*. 1994;8:315–327.
17. Fan JR, Zhao H, Jin J. Two-phase velocity measurements in particle-laden coaxial jets. *Chem Eng J*. 1996;63:11–17.
18. Aisa L, Garcia JA, Cerecedo LM, Garcia PI, Calvo E. Particle concentration and local mass flux measurements in two-phase flows

with PDA. Application to a study on the dispersion of spherical particles in a turbulent air jet. *Int J Multiphase Flow*. 2002;28:301–324.
19. Hadinoto K, Jones EN, Yurteri C, Curtis JS. Reynolds number dependence of gas-phase turbulence in gas–particle flows. *Int J Multiphase Flow*. 2005;31:416–434.
20. Zhou H, Cen KF, Fan JR. Experimental investigation on flow structures and mixing mechanisms of a gas–solid burner jet. *Fuel*. 2005;84:1622–1634.
21. Tamburello DA, Amitay M. Active manipulation of a particle-laden jet. *Int J Multiphase Flow*. 2008;34:829–851.
22. Mergheni MA, Sautet JC, Godard G, Ticha HB, Nasrallah SB. Experimental investigation of turbulence modulation in particle-laden coaxial jets by Phase Doppler Anemometry. *Exp Therm Fluid Sci*. 2009;33:517–526.
23. Kendall JM. Experiments on annular liquid jet instability and on the formation of liquid shells. *Phys Fluids*. 1986;29:2086–2094.
24. Li XG, Shen JH. Experiments on annular liquid jet breakup. *Atomization Sprays*. 2001;11:557–573.
25. Kulkarni V, Sivakumar D, Oommen C, Tharakan TJ. Liquid sheet breakup in gas-centered swirl coaxial atomizers. *ASME Trans J Fluids Eng*. 2010;132:011303-1–011303-7.
26. Sivakumar D, Kulkarni V. Regimes of spray formation in gas-centered swirl coaxial atomizers. *Exp Fluids*. 2011;51;587–596.
27. Sivakumar D, Raghunandan BN. Converging swirling liquid jets from pressure swirl atomizers: effect of inner air pressure. *Phys Fluids*. 2002;14:4389–4398.
28. Leboucher N, Roger F, Carreau JL. Disintegration process of an annular liquid sheet assisted by coaxial gaseous coflow(s). *Atomization Sprays*. 2010;20:847–862.
29. Sevilla A, Gordillo JM, Martinez-Bazan C. Bubble formation in a coflowing air–water stream. *J Fluid Mech*. 2005;530:181–195.
30. Abramoff MD, Magalhaes PJ, Ram SJ. Image processing with ImageJ. *Biophoton Int*. 2004;11:36–42.
31. Toh IK, Honnery D, Soria J. Axial plus tangential entry swirling jet. *Exp Fluids*. 2010;48:309–325.
32. Beer JM, Chigier NA. *Combustion Aerodynamics*. London: Applied Science Publishers, 1972.
33. Kunii D, Levenspiel O. *Fluidization Engineering*. Boston: Butterworth-Heinemann, 1991.
34. Dijkhuizen W, Bokkers GA, Deen NG, van Sint Annaland M, Kuipers, JAM. Extension of PIV for measuring granular temperature field in dense fluidized beds. *AIChE J*. 2007;53:108–118.
35. Andreux R, Chaouki J. Behaviors of the bubble, cloud, and emulsion phases in a fluidized bed. *AIChE J*. 2008;54:406–414.
36. Rudisuli M, Schildhauer TJ, Biollaz SMA, van Ommen JR. Bubble characterization in a fluidized bed by means of optical probes. *Int J Multiphase Flow*. 2012;41:56–67.
37. Movahedirad S, Molaei Dehkordi A, Banaei M, Deen NG, van Sint Annaland M, Kuipers JAM. Bubble size distribution in two-dimensional gas–solid fluidized beds. *Ind Eng Chem Res*. 2012;51:6571–6579.
38. Mudde RF. Bubbles in a fluidized bed: a fast X-ray scanner. *AIChE J*. 2011;57:2684–2690.
39. Santana D, Macias Machin A. Local bubble-size distribution in fluidized beds. *AIChE J*. 2000;46:1340–1347.
40. Ghidaoui MS, Zhao M, McInnis DA, Axworthy DH. A review of water hammer theory and practice. *Appl Mech Rev*. 2005;58:49–76.
41. Lefebvre AH. *Atomization and Sprays*. New York: Hemisphere Publishing Corporation, 1989.

Manuscript received Jun. 12, 2012, and revision received Aug. 27, 2012.